

The higher order leaky Lamb wave sensitivity of a notch in a fluid-immersed plate

Simen Hammervold Midtbø^{a,*}, Svein-Erik Måsøy^a, Magne Aanes^b

^a NTNU, Høgskoleringen 1, Trondheim, 7491, Norway

^b NDT Global, Glasskaret 1, Bergen, 5106, Norway

ARTICLE INFO

Keywords:

Leaky Lamb waves
Crack detection
Sensitivity kernel

ABSTRACT

We present an ultrasonic method of detecting cracks in pipelines based on using normally incident transducers in a pitch-catch setup, which can only excite Lamb modes of higher order than the fundamental modes A_0 and S_0 commonly used in crack detection applications. By excitation and measurements of the Lamb modes S_1 , S_2 , and A_3 , in a steel plate immersed in fluid with and without a notch (to emulate a crack), the performance of the modes towards crack detection is quantified by assessing whether it returns a high leaky component and whether the notch has a large impact on the leaky component. In order to narrow the scope of measurements necessary to investigate notch sensitivity for different system parameters, and to potentially optimize the system setup, we present a computationally efficient theoretical model based on angular spectrum method (ASM) and the theoretical sensitivity kernel formulation from the field of seismology that accounts for a scatterer in the wave path between the transmitter and receiver. The model is compared against measurements, which show that the frequency components of the S_2 mode has both the largest leaky frequency component in the given setup and the largest sensitivity at a frequency close to the maximum leaky frequency such that a difference caused by the notch is easily measured. By using the measurements and the validation calculation as baseline reference, we calculate the expected S_2 mode sensitivity and leaky components for larger plate thicknesses and larger standoffs, which exemplifies how the model can be applied in measurement system design and optimization.

1. Introduction

The detection of cracks or defects in materials using ultrasound is a well-known and exhausted topic of research [1–11]. The continuous development has led to assessment of integrity within a range of industries and materials, for example, composites [1,12], the railway industry [10], and the pipeline industry [3,7,11] where cracks have been a concern due to the risk of explosions [13], and the subsequent waste of valuable energy resources. As a countermeasure to reduce this risk, several ultrasonic testing (UT) methods have been developed for the monitoring of pipelines, using both static (e.g., clamp-on tools) and in-line inspection (ILI) tools in gas or liquid pipelines [6,8,14–16]. The typical approach within UT is to use angled transducers in pulse-echo (PE) or pitch-catch (PC) setup, in order to either excite shear waves in the pipe wall [16,17], or by exciting the fundamental Lamb modes A_0 and S_0 [2,4,6,18], which is the sum of excited compressional and shear waves. A requirement by these methods, however, is that they can only excite and receive the waves by angled transducers, introducing a path dependent directivity, which is either designed to detect axial

or circumferential cracks and thus limits the sensitivity for any crack orientation that is not nearly perpendicular to either of these directions.

An alternative ILI solution that could provide sensitivity within a single tool to both axial, circumferential, and other crack orientations, is to use normally incident transmitters at a distance from the pipe wall [9], which will excite axially symmetric leaky Lamb waves relative to the transmitter. With such a setup, multiple receivers could be positioned in a circumferential order around the transmitter (i.e., PC setup) and would then be able to detect cracks with multiple orientations. Because this can only be achieved with normally incident transmitters, the method can only efficiently excite leaky Lamb waves with mode orders higher than A_0 and S_0 (therefore labeled as 'higher order modes' in this work). The utilization of these leaky Lamb waves has mostly been neglected in crack detection research, though it is shown by Wilcox et al. [4] that in the context of long-range inspection, the higher order modes may suffer from dispersion and high leaky effect. The high leaky effect (or high attenuation, cf. [4]) of higher order modes is also shown in an earlier work [19] by the authors of this

* Corresponding author.

E-mail address: simen.h.midtbø@ntnu.no (S.H. Midtbø).

paper, where especially the thickness-longitudinal modes S_1 and A_3 have a high coupling to the external fluid and thus high leakage. However, in the context of ILI crack detection, the path between a single transmitter- and receiver pair can be minimized to reduce attenuation and to maintain a certain signal-to-noise ratio (SNR), and the spatial resolution within the pipe can be maximized by populating a tool with many transducers. The leaky effect would then rather be exploited for detection of leaky Lamb waves that have either interacted with a notch or not by detecting a change or decrease of transmitted amplitude. The subsequent question then is how sensitive the method is for cracks or crack-like features (e.g., machined notches), which may be highly dependent on the setup parameters, such as excited Lamb mode order and type, wall thickness, geometric distances (e.g., distance between transducers and pipe wall), and notch size. Therefore, a starting point may be to perform a feasibility study by measurements with some of the parameters fixed in order to, for example, limit the scope of which Lamb modes to apply since they may exhibit different properties [4,20] and crack sensitivity. But once this is established, further studies and optimization of sensitivity by measurements alone can be difficult and time consuming considering the vast number of permutations of possible system setup parameters.

Another approach to optimize a system setup and to limit the scope of measurements is instead to utilize calculations of leaky Lamb waves interacting with notches or crack-like features, but depending on calculation method, this can also be time consuming even with simple baseline or clean plate calculations (e.g., 2D COMSOL [19]). Faster models, such as plane wave mode shape analysis [4,5,21], the S-parameter approach [5,21,22], or normal mode expansion techniques [23], are all either based on a plane wave approximation, or for the excitation of fundamental Lamb modes S_0 and A_0 . For a normally incident system setup, the plane wave approach may not be sufficient, as there are known discrepancies if predicting beam characteristics using plane wave theory in leaky Lamb wave excitation [19,24–26], in addition to only being able to excite modes higher than the fundamental Lamb modes.

As an alternative sensitivity modeling approach, the mechanical energy density might be applied, which is also suggested by Wilcox et al. [4] for the fundamental Lamb modes as an indication of depth sensitivity. The use of energy density as the basis of a scattering modeling approach is also applied within the field of seismology by Aki and Richards [27] in studies of surface waves. They derive a perturbation model for Love and Rayleigh waves using a variational principle method where the scattered fields become functional equations of the mechanical kinetic- and strain energy densities of the analytical solutions of the solid equation of motion. Similarly, Snieder [28,29] assumed that the scattered seismic field can be represented as the sum of the wave equation solution of a homogeneous medium and a scatter component (Born approximation), to which is then solved for the scatter component. Various authors have also contributed their calculation method, formulation, and representation in the frequency domain [30–34] of this method, where Zhou et al. [33] introduces the ‘sensitivity kernel’ formulation, which can be interpreted as the ratio between the scatter component and a reference field variable. In its simplest form, the sensitivity kernel is proportional with energy density equations in a solid medium, which is purely based on the propagating wave solutions of the equation of motion of a homogeneous solid. In principle, the case solved by the research in seismology is highly analogous to the case of a leaky Lamb wave interacting with a crack or crack-like feature: a source is radiating waves towards a receiver with a scatterer in the wave path. All though the research within seismology can assume an infinite plane wavefront (plane wave), the expressions are generic functions of energy density, which in turn are solely calculated by analytical expressions of the mechanical particle displacement, stress, and strain. These field variables can be calculated in both the plane wave domain and in the spatial (diffracted) domain, where the latter have been solved by using the angular spectrum method (ASM) in

the aforementioned earlier paper [19] for a transmitter radiating sound towards a homogeneous fluid-immersed plate and is shown to be highly computationally effective compared to COMSOL. This begs the question if this ASM description of the spatial fields within a fluid-immersed plate can be used to implement the sensitivity kernel formulation in order to achieve a computationally efficient optimization model for the sensitivity of cracks and crack-like features.

The aim of this paper is therefore two-folded: We will first investigate the sensitivity of a crack-like feature (machined notch) via measurements by using normally incident pitch-catch setup and by exciting the S_1 , S_2 , and A_3 modes in a fluid-immersed plate. The lateral distance between the transmitter and receiver will be kept to a minimum in order to maintain a high SNR, and both will be positioned at the same distance from the plate. Measurements with and without a notch on the plate will be performed, and the notch will be a 50% depth notch positioned such that it is in the center of the wave path between the transmitter and receiver, oriented perpendicular to the direct wave path, which we consider as a minimum requirement for the quantification of detection ability and sensitivity. The quantification will be based on two criteria; the first will be to examine whether the leaky Lamb modes returns a large leaky component from a clean plate, such that it is measurable in a noisy environment, and the second criteria is whether the notch has a large impact on this leaky component such that any differences due to the notch is also measurable. This impact will be defined as the difference between a measurement with a notch and a measurement without a notch relative to the latter case, where the aim is to limit the scope of Lamb mode candidates in terms of sensitivity. In order to further map the possible system setup by efficient calculations instead of measurements, the second aim of the paper is therefore also to implement the sensitivity kernel model from the field of seismology, by using the formulation by a combination of authors [32,33,35], with necessary modifications in order to represent a sensitivity kernel of the case when a transmitter is radiating sound waves towards a fluid-immersed plate as described in the earlier paper [19]. We will however keep modifications to a minimum such that the sensitivity kernel model is true to the original papers, and is thus considered more as an approximation, or feasibility of utilization, instead of a true solution because of the simple interpretation of the theory. Some examples of the utilization of the theoretical sensitivity kernel in terms of optimization will be shown, with focus on the choice of frequency, transducer-to-plate distance (hereby referred to as ‘standoff’), and the potential in applying this method to larger plate thicknesses by comparing with the baseline measurements and calculations.

As it is necessary to have a pitch-catch model for a clean plate, we will in Section 2 start with the ASM description of the received reflected sound pressure, when a transmitter is radiating sound waves towards a plate from a distance, with a receiver laterally positioned with the same distance to the plate. We then summarize the ASM description of the spatial field variables within the plate itself, which are shown in detail [19], before we then introduce the sensitivity kernel formulation using the theoretical equations of the spatial fields within a plate. In Section 3 we describe the experimental procedure in measurements of a clean plate and the plate with a notch, and the processing and presentation of data. Following this in Section 4, we will go through the calculation parameters and calculation methods, before presenting the measurement and calculation results in Section 5, which will be further discussed in Section 6. At the end in Section 7, we will conclude on the higher order leaky Lamb wave sensitivity of a notch in a fluid-immersed plate, and discuss the further work that is outside the scope of this paper.

2. Theory

We will in Section 2.1 start with the fluid model setup and equations for the case of a clean plate, which is highly analogous to the case of the

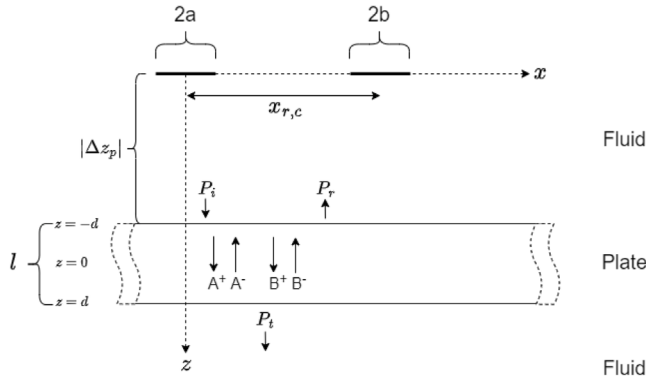


Fig. 1. The setup of a normally incident baffled circular piston radiating a sound pressure P_i towards the plate. The resulting reflected and transmitted sound pressures are P_r and P_t , where the aim is to calculate the reflected sound pressure at the area representing a circular finite receiver. The receiver has a center-to-center distance $x_{r,c}$ from the transmitter, and the y-axis is pointing out of the paper. The lateral positions of the field variables in the illustration are arbitrary.

previous paper [19], but we are here also modeling the reflected field in the fluid at a lateral receiver. Then the theory on the ASM modeling for the field variables within the plate will be summarized in Section 2.2, as it is shown in detail in the previous paper, before ending this section with the sensitivity kernel theory in Section 2.3.

2.1. Fluid

The setup of the clean plate model is shown in Fig. 1, which is similar to the setup shown in [19], but with a finite receiver with radius b positioned such that the center coordinates is $(x, y, z) = (x_{r,c}, 0, z')$ where the transmitter center coordinates are $(x, y, z) = (0, 0, z')$ with radius a . The plate, which is infinitely large along the x- and y-axis, is positioned such that the center coordinate of the plate along the z-axis is 0, with $-d$ as the upper surface coordinate and d as the lower surface coordinate, with a plate thickness of $l = 2d$. In the horizontal wavenumber domain, the reflected and transmitted sound pressures due to the incoming sound pressure P_i are P_r and P_t , respectively, where we are aiming to model the reflected component over the area of the receiver. The coefficients A^+ and A^- represents the amplitudes of the compressional waves propagating between the plate boundaries of the plate due to the incoming sound pressure, while B^+ and B^- represents the shear waves. The solutions of these coefficients are shown in the previous paper [19], and will be summarized in Section 2.2.

The incoming angular spectrum sound pressure at the upper surface of the plate is [19]

$$P_i(\eta, z = -d) = \frac{\rho_f \omega}{h_{f,z}} V_z(\eta) e^{-ih_{f,z}|\Delta z_p|}, \quad (1)$$

where $|\Delta z_p| = |z - z'|$ with $z = -d$ as the upper surface coordinate, ρ_f is the fluid density, and ω is the angular frequency. The independent variable $\eta = |\vec{\eta}|$ is the horizontal wavenumber component in the wavenumber vector $\vec{h}_f = \vec{\eta} + \vec{h}_{f,z}$, where $\vec{h}_{f,z}$ is the vertical fluid wavenumber component with magnitude

$$h_{f,z} = \begin{cases} \sqrt{h_f^2 - \eta^2}, & \eta < h_f, \\ -i\sqrt{\eta^2 - h_f^2}, & \eta > h_f. \end{cases} \quad (2)$$

The spatial sound field in 3D is calculated by doing a Hankel transform as [19]

$$p_i(\vec{r}, z = -d) = \frac{1}{2\pi} \int_0^\infty P_i(\eta, z = -d) J_0(\eta r) \eta d\eta, \quad (3)$$

where $r = |\vec{r}| = \sqrt{x^2 + y^2}$. The reflected and transmitted angular spectrum sound pressure from the plate is calculated by multiplying

the incident angular spectrum, Eq. (1), with the plane wave reflection and transmission coefficients [36–38], where the coefficients are respectively given as [24,38,39]

$$\mathcal{R}(\eta, d) = \frac{AS - Y^2}{(S + iY)(A - iY)}, \quad (4)$$

$$\mathcal{T}(\eta, d) = \frac{-iY(A + S)}{(S + iY)(A - iY)}, \quad (5)$$

with

$$A = (2\eta^2 - k^2)^2 \tan(h_z d) + 4\eta^2 h_z k_z \tan(k_z d), \quad (6)$$

$$S = (2\eta^2 - k^2)^2 \frac{1}{\tan(h_z d)} + 4\eta^2 h_z k_z \frac{1}{\tan(k_z d)}, \quad (7)$$

$$Y = \frac{\rho_f h_z k^4}{\rho_p h_{f,z}}, \quad (8)$$

where ρ_p is the plate density. The vertical compressional wavenumber, h_z , and the vertical shear wavenumber, k_z , are given as

$$h_z = \begin{cases} \sqrt{h^2 - \eta^2}, & \eta < h, \\ -i\sqrt{\eta^2 - h^2}, & \eta > h, \end{cases} \quad (9)$$

$$k_z = \begin{cases} \sqrt{k^2 - \eta^2}, & \eta < k, \\ -i\sqrt{\eta^2 - k^2}, & \eta > k, \end{cases} \quad (10)$$

where $h = \omega/c_l$ and $k = \omega/c_s$, with c_l being the compressional wave speed and c_s the shear wave speed.

The reflected angular spectrum sound pressure at the upper surface of the plate is given by [24,37,38]

$$P_r(\eta, z = -d) = P_i(\eta, z = -d) \mathcal{R}(\eta, d), \quad (11)$$

where $P_i(\eta, r, z = -d)$ is given in Eq. (1). Using plane wave phase extrapolation [40], the reflected angular spectrum sound pressure in the plane of the receiver is [37,41]

$$P_r(\eta, z' = 2|\Delta z_p|) = P_i(\eta, z = -d) \mathcal{R}(\eta, d) e^{-ih_{f,z}|\Delta z_p|}, \quad (12)$$

and the spatial reflected sound pressure in the plane of the receiver is given as [37,41]

$$p_r(\vec{r}, z' = 2|\Delta z_p|) = \frac{1}{2\pi} \int_0^\infty P_r(\eta, z' = 2|\Delta z_p|) J_0(\eta r) \eta d\eta. \quad (13)$$

In order to account for a finite receiver, the spatial field is averaged over the area of an receiver as [38]

$$\langle p_r(z' = 2|\Delta z_p|) \rangle = \frac{1}{2\pi^2 b^2} \int_A p_r(\vec{r}, z') dA, \quad (14)$$

where dA is in the x-y plane. The integration is performed numerically over a circular area with center coordinates at $(x, y, z) = (x_{r,c}, 0, z')$ with radius b .

The reflected sound pressure in Eq. (14) is the sum of both the leaky component from the plate and the specular reflection (surface reflection), such that it can be written as

$$\langle p_r(z' = 2|\Delta z_p|) \rangle = \langle p_{clean,spec}(z' = 2|\Delta z_p|) \rangle + \langle p_{clean,l}(z' = 2|\Delta z_p|) \rangle, \quad (15)$$

where subscript 'spec' denotes specular component and subscript 'l' the leaky component. The calculation can be directly compared with measurements, but we are also interested in calculating the pure leaky component to compare with the notch measurements. We assume that the specular component would be measured as the same if a receiver was positioned such that it faces the transmitter, but at the same lateral position as the receiver in Fig. 1, at twice the distance of $|\Delta z_p|$. This is the same as putting $\mathcal{R} = 1$ in Eq. (12), such that the leaky component will be calculated as

$$\langle p_{clean,l}(z' = 2|\Delta z_p|) \rangle = \langle p_r(z' = 2|\Delta z_p|) \rangle - \langle p_{clean,spec}(z' = 2|\Delta z_p|) \rangle, \quad (16)$$

$$= \frac{1}{2\pi^2 b^2} \int_A \int_0^\infty P_i(\eta, z = -d) [\mathcal{R}(\eta, d) - 1] e^{-ih_{f,z}|\Delta z_p|} J_0(\eta r) \eta d\eta dA. \quad (17)$$

Examples of the difference between the leaky component in Eq. (17) and the reflected component in Eq. (14) will be shown in Section 5.1.

We have now shown the fluid components that arise when radiating sound waves towards the plate, and we next summarize the modeling of the field variables within the plate itself.

2.2. Plate fields

The derivation of the subsequent fields that arises when the incoming pressure field in the fluid interacts with the plate are shown in more detail in [19]. The relevant field variables are here summarized.

We will focus on analysis of the components of mechanical energy density [19]. This relies on the particle displacement, stress, and strain components, where the spatial particle displacement components are calculated as [19]

$$u_r(\vec{r}, z) = \frac{1}{2\pi} \int_0^\infty U_r(\eta, \vec{r}, z) \eta d\eta, \quad (18)$$

$$u_z(\vec{r}, z) = \frac{1}{2\pi} \int_0^\infty U_z(\eta, \vec{r}, z) \eta d\eta, \quad (19)$$

where $u_r(\vec{r}, z)$ is the horizontal displacement component, $u_z(\vec{r}, z)$ is the vertical displacement component, and where $U_r(\eta, z)$ and $U_z(\eta, z)$ are the angular spectrum representation of the horizontal and vertical displacement respectively, which is given as [19]

$$U_r(\eta, \vec{r}, z) = \{-\eta[A_{21} \cos(h_z z) + iA_{22} \sin(h_z z)] + k_z[B_{21} \sin(k_z z) - iB_{22} \cos(k_z z)]\} J_1(\eta r), \quad (20)$$

$$U_z(\eta, \vec{r}, z) = \{-h_z[A_{21} \sin(h_z z) - iA_{22} \cos(h_z z)] + \eta[B_{21} \cos(k_z z) + iB_{22} \sin(k_z z)]\} J_0(\eta r), \quad (21)$$

where J_0 and J_1 are the zeroth and first order Bessel functions, respectively. The spatial stress components are [19]

$$t_{rr}(\vec{r}, z) = \frac{1}{2\pi} \int_0^\infty T_{rr}(\eta, \vec{r}, z) \eta d\eta, \quad (22)$$

$$t_{\theta\theta}(\vec{r}, z) = \frac{1}{2\pi} \int_0^\infty T_{\theta\theta}(\eta, \vec{r}, z) \eta d\eta, \quad (23)$$

$$t_{zz}(\vec{r}, z) = \frac{1}{2\pi} \int_0^\infty T_{zz}(\eta, \vec{r}, z) \eta d\eta, \quad (24)$$

$$t_{rz}(\vec{r}, z) = \frac{1}{2\pi} \int_0^\infty T_{rz}(\eta, \vec{r}, z) \eta d\eta, \quad (25)$$

where the angular spectra representations are [19]

$$\begin{aligned} T_{rr}(\eta, \vec{r}, z) = & -h^2 \lambda_p [A_{21} \cos(h_z z) + iA_{22} \sin(h_z z)] J_0(\eta r) \\ & - 2\mu_p \eta^2 [A_{21} \cos(h_z z) + iA_{22} \sin(h_z z)] \left(J_0(\eta r) - \frac{J_1(\eta r)}{\eta r} \right) \\ & + 2\mu_p k_z \eta [B_{21} \sin(k_z z) - iB_{22} \cos(k_z z)] \left(J_0(\eta r) - \frac{J_1(\eta r)}{\eta r} \right), \end{aligned} \quad (26)$$

$$\begin{aligned} T_{\theta\theta}(\eta, \vec{r}, z) = & -h^2 \lambda_p [A_{21} \cos(h_z z) + iA_{22} \sin(h_z z)] J_0(\eta r) \\ & - 2\mu_p \eta^2 [A_{21} \cos(h_z z) + iA_{22} \sin(h_z z)] \frac{J_1(\eta r)}{\eta r} \\ & + 2\mu_p k_z \eta [B_{21} \sin(k_z z) - iB_{22} \cos(k_z z)] \frac{J_1(\eta r)}{\eta r}, \end{aligned} \quad (27)$$

$$\begin{aligned} T_{zz}(\eta, \vec{r}, z) = & \{\mu_p(2\eta^2 - k^2)[A_{21} \cos(h_z z) + iA_{22} \sin(h_z z)] \\ & - 2\mu_p \eta k_z [B_{21} \sin(k_z z) - iB_{22} \cos(k_z z)]\} J_0(\eta r), \end{aligned} \quad (28)$$

$$\begin{aligned} T_{rz}(\eta, \vec{r}, z) = & \{2\mu_p \eta h_z [A_{21} \sin(h_z z) - iA_{22} \cos(h_z z)] \\ & - \mu_p(2\eta^2 - k^2)[B_{21} \cos(k_z z) + iB_{22} \sin(k_z z)]\} J_1(\eta r), \end{aligned} \quad (29)$$

with μ_p and λ_p as the Lamé constants [27]. The coefficients A_{21} , A_{22} , B_{21} , and B_{22} , are shown in [19] to be

$$A_{21} = \frac{-(2\eta^2 - k^2)P_i(\mathcal{T} + \mathcal{R} + 1)}{\mu_p 2S \sin(h_z d)}, \quad (30)$$

$$A_{22} = \frac{i(2\eta^2 - k^2)P_i(\mathcal{T} - \mathcal{R} - 1)}{\mu_p 2A \cos(h_z d)}, \quad (31)$$

$$B_{21} = \frac{h_z \eta P_i(\mathcal{T} - \mathcal{R} - 1)}{\mu_p A \cos(k_z d)}, \quad (32)$$

$$B_{22} = \frac{i h_z \eta P_i(\mathcal{T} + \mathcal{R} + 1)}{\mu_p S \sin(k_z d)}, \quad (33)$$

where \mathcal{R} and \mathcal{T} is the reflection- and transmission coefficient in Eqs. (4) and (5), respectively, while P_i is the incoming angular spectrum pressure in Eq. (1). As in the previous paper [19], the calculation of the strain components will be performed by expressing them as functional equations of the stress to increase computational efficiency. The spatial strain components are given as [19]

$$s_{rr}(\vec{r}, z) = \frac{(\lambda_p + 2\mu_p)[\lambda_p(t_{zz} + t_{\theta\theta}) - 2t_{rr}(\lambda_p + \mu_p)]}{2\mu_p[\lambda_p^2 - 4(\lambda_p + \mu_p)^2]}, \quad (34)$$

$$s_{\theta\theta}(\vec{r}, z) = \frac{(\lambda_p + 2\mu_p)[\lambda_p(t_{zz} + t_{rr}) - 2t_{\theta\theta}(\lambda_p + \mu_p)]}{2\mu_p[\lambda_p^2 - 4(\lambda_p + \mu_p)^2]}, \quad (35)$$

$$s_{zz}(\vec{r}, z) = \frac{(\lambda_p + 2\mu_p)[\lambda_p(t_{rr} + t_{\theta\theta}) - 2t_{zz}(\lambda_p + \mu_p)]}{2\mu_p[\lambda_p^2 - 4(\lambda_p + \mu_p)^2]}, \quad (36)$$

$$s_{rz}(\vec{r}, z) = \frac{t_{rz}}{2\mu_p}. \quad (37)$$

With these field variables we are aiming to calculate the sensitivity kernel for this setup when a notch is in the middle of the wave path between the transmitter and receiver in the plate. The derivation of the sensitivity kernel follows in the next subsection.

2.3. The theoretical scatter component

We rely on the perturbation theory and Born approximation from the field of seismology, describing perturbation of surface waves due to lateral heterogeneities [28,29,32,33,35]. This is based on the equation of motion for the general case in a solid with a point force as [35]

$$\mathbf{F} = \rho_p \frac{\partial^2 \mathbf{u}}{\partial t^2} - \nabla[\lambda_p(\nabla \cdot \mathbf{u})] - \nabla \cdot \{\mu_p[(\nabla \mathbf{u}) + (\nabla \mathbf{u})^T]\} = \mathcal{L}\mathbf{u}, \quad (38)$$

where the notation differs from [35] by using a vector notation for an unknown displacement \mathbf{u} , instead of tensor notation via the Green's tensor. We also assume that the particle displacement vector consists of the spatial representation components, Eqs. (18)–(19). The last term, $\mathcal{L}\mathbf{u}$, is the operator notation defined in [29], which is useful for the sake of brevity.

The Born approximation is applied in both the displacement and in the operator as [29,35]

$$\mathbf{u} \rightarrow \mathbf{u} + \delta\mathbf{u}, \quad (39)$$

$$\mathcal{L} \rightarrow \mathcal{L} + \delta\mathcal{L}, \quad (40)$$

where the operator perturbation introduces the parameter perturbations (e.g., solid density becomes $\rho_p \rightarrow \rho_p + \delta\rho_p$). Inserting these into Eq. (38), gives the equality [29,35]

$$\mathcal{L}\mathbf{u} + \mathcal{L}\delta\mathbf{u} + \delta\mathcal{L}\mathbf{u} + \delta\mathcal{L}\delta\mathbf{u} = \mathbf{F}, \quad (41)$$

where the left most term cancels with the force term on the right side. The second order perturbation is also neglected, which gives

$$\mathcal{L}\delta\mathbf{u} = -\delta\mathcal{L}\mathbf{u}. \quad (42)$$

This essentially states that the solution of the wave equation for the perturbed displacement is equal to the negative of the wave equation solution when the parameters are regarded as perturbed. For the solution of Eq. (42), Zhao et al. [35] and Snieder [28] refers to the representation theorem of Aki & Richards [27] (which also utilizes the reciprocity theorem [27]), as [28,29,32,35]

$$\delta u = \int_{V_s} \mathbf{u}'' \cdot (-\delta\mathcal{L}\mathbf{u}') dV_s, \quad (43)$$

where the double prime denotes the free field displacement from the scatterer to the receiver, while the single prime denotes the equivalent from the source to the scatterer. Zhao and Dahlen [35] gives Eq. (43) as a convolution between a point force term $(-\delta\mathcal{L}\mathbf{u}')$ and a displacement term (\mathbf{u}'') , where an interpretation is that the scattered field can be regarded as the convolution between a point force and an outgoing displacement, where the point force is a function of the incoming displacement \mathbf{u}' .

The variable separating these two quantities is simply the travel path with $\mathbf{u}' = \mathbf{u}(\vec{\mathbf{r}}'_s, z_s)$ and $\mathbf{u}'' = \mathbf{u}(\vec{\mathbf{r}}''_s, z_s)$, where z_s is the position of the scatterer along the thickness of the plate with $-d \leq z_s \leq d$. Furthermore, using that

$$-\delta\mathcal{L}\mathbf{u}' = \delta\rho_p\omega^2\mathbf{u}' + \nabla[\delta\lambda_p(\nabla \cdot \mathbf{u}')] + \nabla \cdot \{\delta\mu_p[(\nabla\mathbf{u}') + (\nabla\mathbf{u}')^T]\}, \quad (44)$$

the solution, Eq. (43), can be written as [35]

$$\begin{aligned} \delta u = & \int_{V_s} \delta\rho_p\omega^2\mathbf{u}'' \cdot \mathbf{u}' dV_s \\ & + \int_{V_s} \mathbf{u}'' \cdot \nabla[\delta\lambda_p(\nabla \cdot \mathbf{u}')] dV_s \\ & + \int_{V_s} \mathbf{u}'' \cdot (\nabla \cdot \{\delta\mu_p[(\nabla\mathbf{u}') + (\nabla\mathbf{u}')^T]\}) dV_s. \end{aligned} \quad (45)$$

In order to remove the differentiation of the perturbed quantities, $\delta\lambda_p$ and $\delta\mu_p$, the last two terms can be rewritten using Gauss' theorem and partial integration [28,35], and δu becomes

$$\begin{aligned} \delta u = & \int_{V_s} \frac{\delta\rho_p}{\rho_p} [\rho_p\omega^2\mathbf{u}'' \cdot \mathbf{u}'] dV_s \\ & - \int_{V_s} \frac{\delta\lambda_p}{\lambda_p} [\lambda_p(\nabla \cdot \mathbf{u}'')(\nabla \cdot \mathbf{u}')] dV_s \\ & - \int_{V_s} \frac{\delta\mu_p}{\mu_p} \{\mu_p(\nabla\mathbf{u}'') : [(\nabla\mathbf{u}') + (\nabla\mathbf{u}')^T]\} dV_s, \end{aligned} \quad (46)$$

where it is important to note that the Gauss' theorem and partial integration introduces a surface integral which Snieder [28] shows to be zero. We have chosen to show the perturbed model, Eq. (46), using the perturbed fractional model representation [33,35], which is also used by Aki & Richards [27] in their variational technique of describing surface wave perturbations. The first term in Eq. (46) shows that the weight function [27] for $\delta\rho_p/\rho_p$ – the term inside the brackets – is twice the kinetic energy density if $\mathbf{u}'' = \mathbf{u}'$. Similarly, the second term is the square of the summed diagonal strain components if $\mathbf{u}'' = \mathbf{u}'$, which have been referred to as the ‘dilatation’ in the literature (e.g., Bernard et al. [42]), and the third term can be regarded as two times the double dot product of the strain tensor due to its symmetry properties. In other words, the theoretical calculation of the scatter component is essentially energy calculations integrated over a finite sized scatterer, and because of this, we will use δe as notation of Eq. (46), instead of δu . In addition, by using the definition of the Lamé constants [24,27], we can assume that the relationship between the perturbed quantities in Eq. (46) are [33,35]

$$\delta\mu_p = 2\rho_p c_s \delta c_s + c_s^2 \delta\rho_p, \quad (47)$$

$$\delta\lambda_p = 2\rho_p c_l \delta c_l - 4\rho_p c_s \delta c_s - 2c_s^2 \delta\rho_p + c_l^2 \delta\rho_p, \quad (48)$$

such that Eq. (46) (with δe as notation) becomes [33]

$$\begin{aligned} \delta e = & \int_{V_s} \frac{\delta\rho_p}{\rho_p} [\rho_p(2c_s^2 - c_l^2)(\nabla \cdot \mathbf{u}')(\nabla \cdot \mathbf{u}'') - 2\rho_p c_s^2 (\mathbf{s}' : \mathbf{s}'') + \rho_p\omega^2\mathbf{u}' \cdot \mathbf{u}''] dV_s \\ & - \int_{V_s} \frac{\delta c_l}{c_l} [2\rho_p c_l^2 (\nabla \cdot \mathbf{u}')(\nabla \cdot \mathbf{u}'')] dV_s \\ & + \int_{V_s} \frac{\delta c_s}{c_s} [4\rho_p c_s^2 (\nabla \cdot \mathbf{u}')(\nabla \cdot \mathbf{u}'') - 4\rho_p c_s^2 (\mathbf{s}' : \mathbf{s}'')] dV_s, \end{aligned} \quad (49)$$

where \mathbf{s} is the strain tensor. We will be concerned about the density perturbation weight, which is the first term in Eq. (49). In addition, we

will assume that the perturbed quantity $\delta\rho_p$ is independent of spatial position and can therefore be put outside the volumetric integral. The weight can also be rewritten to a more familiar form as

$$\delta e_p = \frac{\delta\rho_p}{\rho_p} \int_{V_s} [\rho_p\omega^2\mathbf{u}' \cdot \mathbf{u}'' - (\mathbf{s}' : \mathbf{t}'')] dV_s, \quad (50)$$

where \mathbf{t} is the stress tensor. Again, if $\mathbf{u}'' = \mathbf{u}'$, the double dot product of the strain and stress can be recognized as twice the strain energy density, while the entire integrand can be recognized as twice the Lagrangian density [27], defined as the kinetic energy minus the strain energy density [27].

We next describe some of the assumptions that are applied in the calculation of Eq. (50), in order to be consistent with the theory from the literature while also applying it for the measurement setup described in this paper.

2.4. Calculating assumptions

The primed particle displacement is defined as $\mathbf{u}' = \mathbf{u}(\vec{\mathbf{r}}'_s, z_s)$ where $r' = |\vec{\mathbf{r}}'_s| = \sqrt{(x_s - x_t)^2 + (y_s - y_t)^2}$ is the lateral path with (x_t, y_t) as the center coordinate of the transmitter and with (x_s, y_s) as the lateral coordinate of the scatterer. Analogously, the double primed particle displacement is defined as $\mathbf{u}'' = \mathbf{u}(\vec{\mathbf{r}}''_s, z_s)$ with $r'' = |\vec{\mathbf{r}}''_s| = \sqrt{(x_s - x_{r,c})^2 + (y_s - y_{r,c})^2}$, where $(x_{r,c}, y_{r,c})$ is the center coordinates of the receiver. The first dot product in Eq. (50) is

$$\mathbf{u}' \cdot \mathbf{u}'' = u'_r u''_r \hat{r}' \cdot \hat{r}'' + u'_z u''_z, \quad (51)$$

where the unit vectors in the lateral direction are allowed to point in different directions [33], where \hat{r}' points in the direction of the path between the transmitter and scatterer, while \hat{r}'' points in the direction of path between scatterer and receiver [33], cf. Fig. 2. The dot product $\hat{r}' \cdot \hat{r}''$ will be calculated as

$$\hat{r}' \cdot \hat{r}'' = \cos \alpha = \frac{\vec{r}'' \cdot \vec{r}'}{|\vec{r}''||\vec{r}'|} = \frac{(x_s - x_t)(x_s - x_{r,c}) + (y_s - y_t)(y_s - y_{r,c})}{\sqrt{(x_s - x_t)^2 + (y_s - y_t)^2} \sqrt{(x_s - x_{r,c})^2 + (y_s - y_{r,c})^2}}, \quad (52)$$

because the angle between the two paths \vec{r}'' and \vec{r}' is the same as between the two unit vectors. Similarly for the last term in Eq. (50), the double dot product will be calculated as

$$\mathbf{s}' : \mathbf{t}'' = s'_{zz} t''_{zz} + 2s'_{rz} t''_{rz} \cos \alpha, \quad (53)$$

where we assume that only the normal- and shear components of the strain energy density contributes to the difference, similar as the assumption that Lowe et al. [5] applies in order to calculate the approximate notch reflection for the A_0 mode, though by only including the axial and shear terms.

The integration in Eq. (50) will be performed across the depth and length of the notch, in two dimensions, assuming that the notch is infinitely thin. The notch will be assumed to be rectangular shaped across depth and length, such that the volumetric integral in Eq. (50) becomes

$$\delta e_p = \frac{\delta\rho_p}{\rho_p} \int_0^d \int_{-n_s}^{n_s} [\rho_p\omega^2\mathbf{u}' \cdot \mathbf{u}'' - (\mathbf{s}' : \mathbf{t}'')] dy_s dz_s, \quad (54)$$

where n_s is half the notch length, and where the notch depth is evaluated and integrated from the middle of the plate $z_s = 0$ to the positive plate boundary $z_s = d$.

Finally, it is necessary to note that Eq. (54) represent the difference of energy within the plate, while we are mainly concerned with the external energy arriving at a finite receiver in the fluid medium. The calculation input accounting for the distance between source and plate of both primed and double primed field variables in the scatter component, Eq. (50), is the incoming angular spectrum sound pressure, Eq. (1), in the coefficients Eqs. (30)–(33). These are functions of the

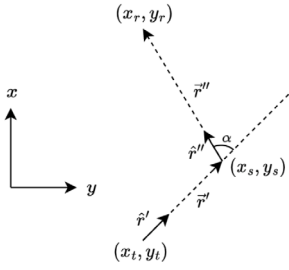


Fig. 2. The geometry and paths between the transmitter, scatterer, and the receiver.

vertical distance $|\Delta z_p|$, while the total vertical propagation path at the receiver in the measurements and calculations of the reflected component will be $2|\Delta z_p|$ (cf. Eq. (14) and Eq. (17)). We will therefore simply assume that this can be compensated by doubling the distance in the input of the scatter component by using $2|\Delta z_p|$ in the exponential term of the incoming angular spectrum sound pressure P_i in Eqs. (1) and (30) – (33). Alternatively, it could be possible to find an equivalent expression of the scatter component in the fluid medium, though this derivation has not been attempted in this paper. A starting point however could be the law of energy balance [43,44].

3. Experimental setup and method

This section will describe the mechanical and electrical setup of the measurements, the measurement and processing procedure, and some of the technical difficulties in fully comparing measurements with calculations.

3.1. Setup

The plate measurements were performed using a XYZ scanner (Precision Acoustics), which consist of a metal framework with motorstages to move a mechanical arm in the three dimensions. A transducer holder was attached at the end of the arm with a single transducer pair from Imasonic with 16 mm active diameter surface with center frequency at 950 kHz, with an operating bandwidth between 450 kHz to 1460 kHz (−6 dB limits). The center-to-center distance between the transducer faces was $x_{r,c} = 40$ mm, which was chosen as a compromise between having a sufficient amplitude of the leaky component and low magnitude of the specular component to reduce its influence. It is however expected that the energy of the thickness-longitudinal modes will decay significantly within this distance, as shown in the previous paper [19]. The standoff was set to $|\Delta z_p| = 80$ mm, and the distance from the centers of both the transducers to the center of the notch in the lateral direction was 20 mm. The transducers were positioned such that the lateral sound path between them was perpendicular to the notch orientation. Both a measurement without a notch (clean plate) and with a notch was performed for the same parameters and frequencies. In order to be consistent with the theoretical setup, where the received sound in a single side pitch-catch system (Fig. 1) is calculated using the plane wave reflection coefficient, the measurement will be referred to as ‘measured reflection component’, and if a notch is present, as ‘measured reflection component with a notch’.

The XYZ scanner communicates with software from Precision Acoustics on a PC and oscilloscope (Keysight InfiniiVision), with the trigger connected to a Tenma 72-3555 signal generator. The generated signal was a 64 cycle sine, with $1 V_{pp}$ as input voltage to the transmitter. The received signal was amplified using a 40 dB HVA-10M-60-F amplifier (Precision Acoustics) connected to the oscilloscope.

The plate used in the measurements was a 4.02 mm thick stainless steel plate with grade AISI 316L, consisting of a notch with 50 mm length, with an elliptically shaped depth with 50% maximum of the

plate thickness. A digital angle gauge was used to ensure that the plate, the notch, and the transducer holder along with transducer faces were as aligned and perpendicular as possible.

The cut-off frequencies [19,24] within the transducer bandwidth for the higher Lamb modes for a 4.02 mm thick plate are

$$\begin{aligned} f_{l1}^S &= f_{S1} = 719 \text{ kHz}, \\ f_{l1}^S &= f_{S2} = 779 \text{ kHz}, \\ f_{l2}^A &= f_{A2} = 1168 \text{ kHz}, \\ f_{l1}^A &= f_{A3} = 1438 \text{ kHz}, \end{aligned}$$

where we have excluded, for example, $A_1 = 389$ kHz and any higher order modes than A_3 since they will be outside the operating bandwidth of the transducer. In addition, performing accurate measurements of the A_2 mode was deemed to difficult, as it exists for a very narrow frequency area. This can be further illustrated by examining the dispersion curves [19,24] of the Lamb modes, which are shown in Fig. 3 as a function of frequency and incident angle for a 4.02 mm stainless steel plate in water (medium parameters are given in Section 4). The cut-off frequencies are the frequencies where the angle of incidence is 0° . In the figure, the −3 dB angle for the frequencies near S_1 and S_2 of the transducers used in the measurements is marked with a black vertical line at roughly 3.4° , which can be used to exemplify how the incoming normally incident beam will excite the two modes and why plane wave theory is an insufficient description. For example, by examining the S_1 curve, the mode will be excited for frequencies lower than the cut-off frequency [19,24,25] due to the incident beam, since the curve has a slope that exists for frequencies lower than the cut-off frequency and because the incident beam has an angular distribution of energy as indicated by the −3 dB angle. A normally incident plane wave at 0° would predict the excitation of S_1 at its cut-off frequency [24]. Similarly, but for the S_2 mode, it may be excited for frequencies higher than the cut-off frequency. For the A_2 mode, the dispersion curve is almost constant for all angles between 0° and 6° , with a −3 dB angle at 2.3° , meaning that it will be excited for a very narrow frequency band around its cut-off frequency at 1168 kHz. Note how the curves of the A_0 mode and S_0 mode show that they cannot be efficiently excited unless tilting the transmitter and receiver, though with a finite beam at normal incidence, the modes might be excited to some extent, at least in terms of the angular spectrum (e.g., see angular spectrum calculations in [24]).

We are in this paper focusing on the frequency that returns the largest leaky component for the particular Lamb mode, and the frequency areas were therefore chosen such that they cover the frequency spectrum peaks in the vicinity of the cut-off frequency [19], but where the leaky effect and therefore the measured response is highest. The frequency components of maximum leakage for the S_1 , S_2 , and A_3 modes will be shown in Section 5, and the frequency areas were chosen as 680–730 kHz, 780–830 kHz, and 1435–1470 kHz, respectively.

3.2. Processing of measurements

The measurements were transformed to the frequency domain using a Fast Fourier transform of the steady state time window. Then, in an attempt to quantify the impact of a notch, it was assumed that a measurement when a notch is present can be represented by the superposition of a clean component (direct component) and a scatter component (i.e. Born approximation [32,33]), on the form

$$p_{notch} = p_{clean} + \Delta p, \quad (55)$$

where p_{clean} is the clean component, and Δp is the scatter component. If this is solved for Δp , the signals can be further decomposed into its leaky and specular components as

$$\Delta p = p_{notch,l} + p_{notch,spec} - p_{clean,l} - p_{clean,spec}. \quad (56)$$

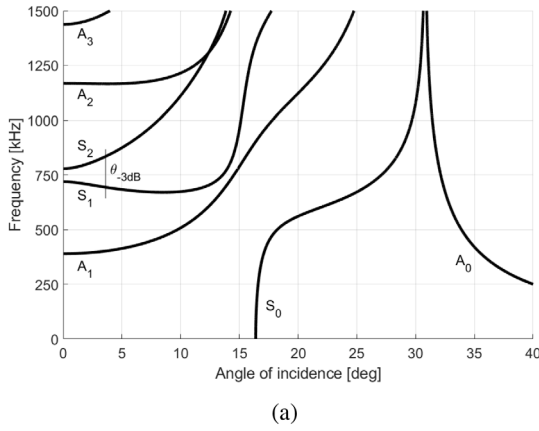


Fig. 3. The dispersion curves of Lamb modes in a 4.02 mm thick plate as a function of frequency and incident angle with water as medium. The vertical line indicates the -3dB angle of the transducers near the frequencies of the S_1 and S_2 mode.

But in an ideal measurement the specular reflection component can be assumed to be equal in the two measurements, so

$$\Delta p = p_{\text{notch},l} - p_{\text{clean},l}, \quad (57)$$

and the quantity should represent the pure differences in leakiness. If we also normalize this to the leaky clean plate component as

$$\frac{\Delta p}{p_{\text{clean},l}} = \frac{p_{\text{notch},l} - p_{\text{clean},l}}{p_{\text{clean},l}}, \quad (58)$$

we have now defined the relative difference for a measurement with a notch and a measurement without a notch, which will be used to quantify the impact of a notch. This is also the definition of the theoretical sensitivity kernel, defined as the ratio of the scatter component and a reference component [33,45], where we will refer to the measurement as 'measured sensitivity kernel'. Note that whenever the measured sensitivity kernel is close to 0, the two measurements in the numerator are approximately equal, and the notch is essentially invisible to the system. If the $p_{\text{notch},l}$ value component is small due to the presence of a notch, which indicates that the transmitted wavefield through the notch is small, the magnitude of the difference in the numerator should be close to the clean plate value and the measured sensitivity kernel will be close to 1. Since the difference in the numerator includes phase information, the measured sensitivity kernel can in principle be larger than 1.

Ideally, the leaky clean plate component, $p_{\text{clean},l}$, should be measured separately by also measuring the specular component component and subtracting it from the reflected field, $p_{\text{clean},r}$, similarly as is done in calculations, cf. Eq. (17). The specular component could be measured by the same assumption in the calculations, by using a mirrored receiver technique with the receiver face in the opposite direction of the transmitter but positioned at a lateral distance corresponding to the plate measurements, with twice the vertical distance as the receiver to the plate. It proved however difficult in practice, as the current measurement setup does not allow for the measurement without larger alterations on the setup, and thus making it difficult to reproduce the specular component and the corresponding phase as it is in the measurements with a plate. The clean leaky component will therefore be calculated with the ASM model instead from Eq. (17), and the denominator of Eq. (58) changes to

$$\frac{\Delta p}{p_{\text{clean},l}} = \frac{p_{\text{notch},l} - p_{\text{clean},l}}{\langle p_{\text{clean},l} \rangle}. \quad (59)$$

For true validation of the calculated scatter component δe however, we will normalize the measured Δp component to the measured reflected component without a notch which includes both specular and leaky

component, and compare with the equivalent ratio by the theoretical models.

In order to remove source/receiver sensitivity, both the measurements and calculations are normalized to the case without a plate when a transmitter is radiating sound towards a receiver, with the receiver placed parallel and directly across the transmitter with zero lateral distance at a vertical propagation distance of 160 mm. This method is similar to normalization techniques used in earlier literature (e.g., [24,26]), but is in this work only meant to remove transducer properties such that the results are generalized. The three measurements – the reference measurement, the clean plate measurement, and the measurement of a plate with a notch – are illustrated in Fig. 4.

4. Calculation procedure

The calculation procedure of the calculation of the field variables used in the theoretical sensitivity kernel is described in [19], though it is necessary to specify the parameters used in the calculations in this work for comparisons with measurements.

The immersion fluid is water with density $\rho_f = 1000 \text{ kg m}^{-3}$, with speed of sound $c_f = 1485 \text{ m s}^{-1}$. The stainless steel plate has a density of $\rho_p = 8000 \text{ kg m}^{-3}$ [24] with compressional wave velocity $c_l = 5780 \text{ m s}^{-1}$ [24] and shear wave velocity $c_s = 3130 \text{ m s}^{-1}$ [24], and a thickness of $d = 4.02 \text{ mm}$. The effective radius of the transmitter and receiver used in the measurements was found using a directivity measurement setup and calculated as described by Aanes [24]. For the lower frequencies of the S_1 and S_2 modes, the radii was found to be $a = 8 \text{ mm}$ and $b = 7.5 \text{ mm}$, while for the higher frequencies near A_3 they were $a = 9 \text{ mm}$ and $b = 8.5 \text{ mm}$. The distance between the transmitter and receiver center was 40 mm.

The calculation of the theoretical scatter component, Eq. (54), is performed by calculating the individual stress, strain, and displacement components given in Section 2.2 with the notch placed in the middle between the transmitter and receiver centers with a distance of 20 mm to the center of the notch. The integration was performed for a scatterer of length 50 mm with center coordinates of $(x_{s,c}, y_{s,c}) = (20 \text{ mm}, 0 \text{ mm})$, with a depth of 2.01 mm corresponding to 50% of the plate. As also discussed in Section 2.4, the standoff to the incoming sound pressure is set to twice the distance as the actual standoff in the measurement as $2|\Delta z_p| = 160 \text{ mm}$.

All calculations were performed on a 2.9 GHz computer with 32 GB RAM. As specified in [19], the independent variable η needs sufficient resolution in order to avoid undersampling effects. In this paper, it was sampled with a resolution of minimum $N = 8192$ points. In terms of computing time, for the scatter component calculations, Eq. (54), a calculation for a single frequency and the parameters specified above used approximately 3 s.

5. Results

In Section 5.1, we first present the measurements of the reflected response from a clean plate compared with calculations, before an equivalent measurement, but with a notch present, is shown in Section 5.2 with the sensitivity kernel formulation. We then compare the theoretical sensitivity kernel calculations with the measured in Section 5.3, and then use these results as baseline to compare sensitivity kernel calculations with larger plate thicknesses and larger standoffs in Section 5.4.

5.1. Reflected and leaky component from clean plate

The result of the clean plate measurements and calculations are shown in Fig. 5, where the calculated clean leaky component (Eq. (17)) is compared against both the measured and calculated reflected components (Eq. (14)), along with the calculated specular reflection (Eq. (14))

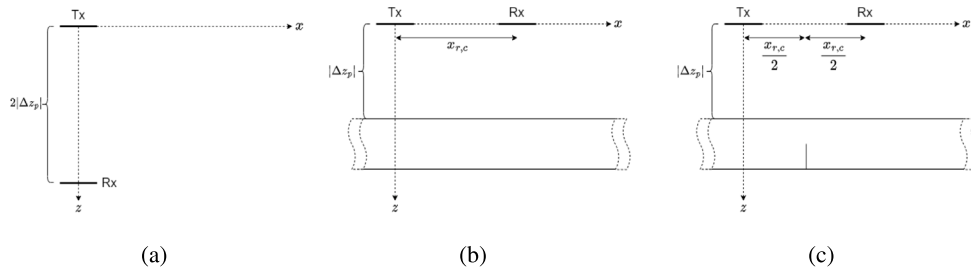


Fig. 4. Unscaled 2D illustration of the 3 measurements performed, where (a) shows the reference measurement setup, (b) shows the clean plate measurement setup, and (c) shows the setup for the plate with a notch.

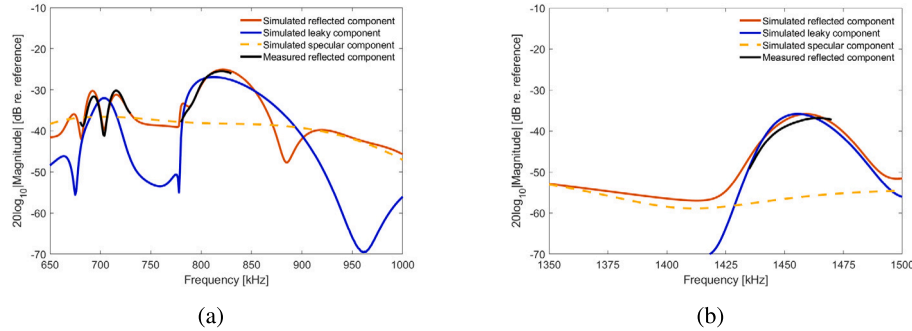


Fig. 5. The calculated reflected, leaky, and specular components, compared with the measured reflected component, where (a) shows the frequency area for both the S_1 and S_2 modes, while (b) shows the A_3 mode frequency area. All measurements and calculations are normalized to the reference measurement of a receiver placed directly across the transmitter at a distance of 160 mm.

with $\mathcal{R}(\eta, d) = 1$) for the frequency areas of S_1 (680–730 kHz), S_2 (780–830 kHz) and A_3 (1435–1470 kHz).

The clean plate leaky components is shown to differ in shape and magnitude from the reflected components, perhaps most significantly for the frequencies of the S_1 mode. The calculated specular component has the highest magnitude relative to the leaky component in the frequency area of S_1 , indicating that it will interfere more significantly with the leaky component in this frequency range than at the higher frequencies. The leaky component is largest for the frequencies of the S_2 mode, with a peak frequency at 813 kHz, which is 5 dB higher than the peak frequency magnitude of S_1 at 704 kHz, and 9 dB higher than the peak frequency magnitude of A_3 at 1456 kHz.

Out of the three frequency areas, the measurement of the frequency components of the A_3 mode differs most significantly from the calculations, presumably due to the sensitivity of a small misalignment that may be introduced for high frequencies and consequentially high directivity. However, it also shows practically no difference between the leaky component and the reflected component close to the cut-off frequency because of the high directivity and therefore little impact from the sidelobes and its specular component.

The comparison of the clean plate measurements and calculations for the reflected component shows a similar trend, which implies that the calculated leaky component can be used to represent the clean leaky component in the denominator of the measured sensitivity kernel, as discussed in Section 3. Next, we present the Δp measurements and sensitivity kernel with a notch centered between the transmitter and the receiver, and the impact on leakiness for the different Lamb modes.

5.2. The measured sensitivity kernel

In the left column of Fig. 6, the measured Δp component is compared against the calculated leaky component (Eq. (17)), the measured reflected component with a notch, and the measured reflected component without a notch. Note that the difference of the two latter measurements gives the Δp component, though by their complex values

and not the individual absolute values as presented in the figure. The resulting ratios between the Δp and both the calculated leaky component and the measured reflected component without a notch are shown in the right column. Each row, from top to bottom, shows the S_1 , S_2 , and A_3 frequency areas, respectively. The calculated leaky components and the measured reflected field without a notch are the same as shown in Figs. 5(a) and 5(b), but the figure dynamics are changed to give a more detailed comparison with the measured Δp component. As stated in Section 3, the ratio between the Δp component and the leaky component represent the measured sensitivity kernel of interest in this work (Eq. (59), blue–green color in right column of Fig. 6), while the ratio between the Δp component and the measured reflected component without a notch is to be used for validation of the theoretical calculations of the equivalent ratio in the next subsection.

For the measured sensitivity kernel and frequency components of S_1 , Fig. 6(b), the magnitude is largest for the lowest of frequencies, indicating a higher sensitivity for these frequencies. This is also indicated by the similar magnitude between the simulated leaky component and the Δp component in Fig. 6(a), indicating that the transmitted wave through the notch is small, as discussed in Section 3.2. However, this is also at a frequency where the leaky field is 13 dB lower than the peak frequency at 704 kHz. The measured reflected component with a notch shows different behavior compared to the measurement without a notch, but it is difficult to assess the impact of a notch, considering the difference is caused by a combination of different physical mechanisms; both a potential amplitude change and phase change of the leaky component due to the presence of a notch will interfere with the specular component, which is dependent on the surface properties, and its amplitude and phase might therefore vary.

For the measured sensitivity kernel of the frequencies of S_2 in Fig. 6(d), it also shows a high sensitivity for the lowest frequency where the leaky component is 15 dB lower than its peak frequency value at 813 kHz (cf. Fig. 6(c)), though with an additional peak of sensitivity at 799 kHz. At this frequency, the leaky component is 1 dB less than the peak value, which therefore shows both high sensitivity for the

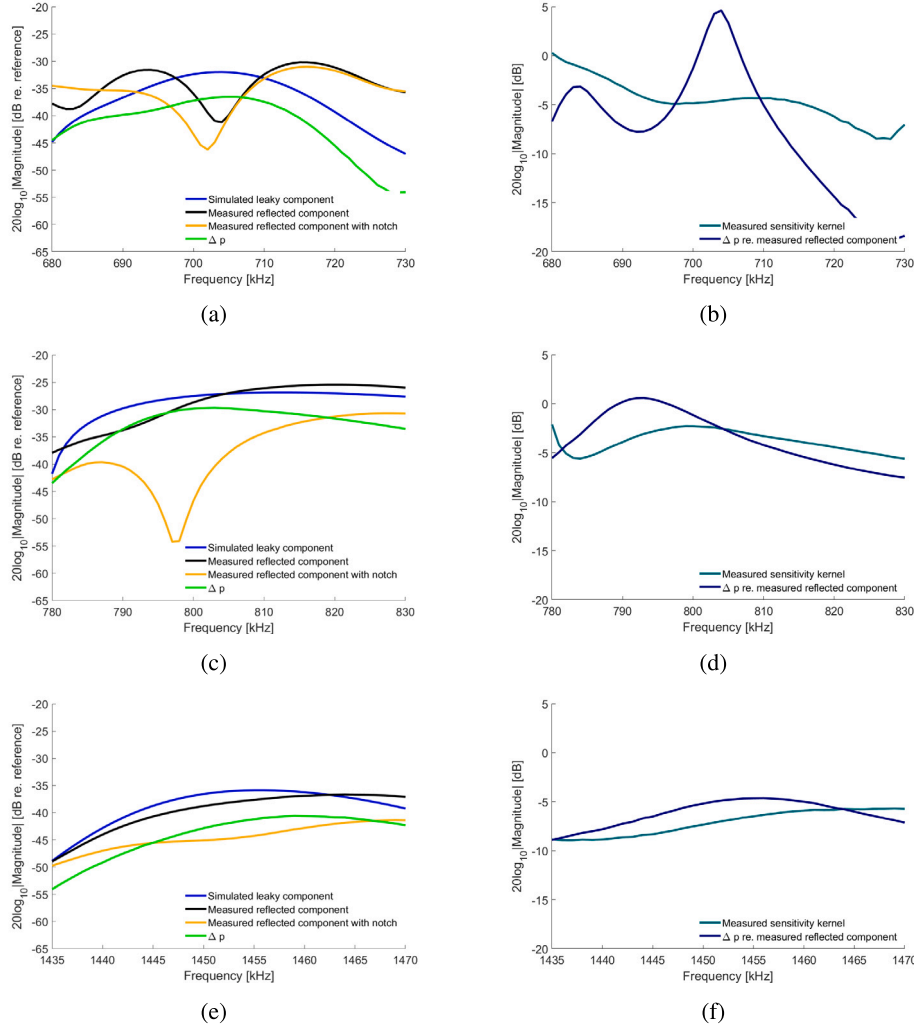


Fig. 6. The left column shows the calculated leaky component, the measured reflected component, the measured reflected component with a notch, compared to the measured Δp . All curves are normalized to the reference at 160 mm, and the right column shows the resulting sensitivity kernel (Eq. (59)) along with the ratio of the measured Δp component and the reflected component. The top row, (a) and (b), shows the spectrum of the frequencies of S_1 ; (c) and (d) of S_2 ; and (e) and (f) of A_3 .

notch and a high magnitude leaky component. The measured sensitivity kernel for the frequencies of A_3 , shown in Fig. 6(f), has a low sensitivity and leaky magnitude compared to the other modes across all frequency components.

The frequency components of the S_2 mode shows the largest leaky component peak, in addition to a large sensitivity in the vicinity of this peak, and is therefore the most suitable leaky Lamb mode in this work as per the criteria set in Section 1. We will however in the next section show comparison of calculations and measurements for all the three frequency areas for the sake of completeness and to illustrate the limitations with the theoretical sensitivity kernel.

5.3. The theoretical scatter component and sensitivity kernel

A fundamental difference between the theoretical scatter component, δe in Eq. (54), and measured, Δp in Eq. (57), is the measure of difference: the calculated kernel is the difference of energies while the measured difference is the difference of sound pressure. However, we will assume that the difference of energy within the plate in the calculation is the same as the difference of sound pressure in the measurements, such that $\delta e = \Delta p$.

In Fig. 7, the calculated δe normalized to the calculated reflected field for the three frequency areas are compared against the measured equivalent ratios, where each calculation is shifted to fit the maximum of the measurement. As noted in Section 3, these ratios represents a pure comparison between a measured ratio, which removes both source and receiver sensitivity, and a calculated ratio, which should reveal any model- or measurement uncertainties. In the comparison of frequency components in the S_1 region, Fig. 7(a), these uncertainties especially reveal themselves as a large discrepancy for the lower frequencies. On the other hand, for the S_2 and A_3 regions in Fig. 7(b) and Fig. 7(c) respectively, the overall trend between measurement and calculation is similar, except for some discrepancy between the lower frequency area of the S_2 mode, and the higher frequencies for the A_3 mode. As shown in the previous section, we will be mainly concerned with the frequency components of the S_2 mode considering these show both highest sensitivity and measurable leaky component, but these comparisons show a clear example of limitations that the theoretical scatter component introduced in this paper may have. The uncertainties and discrepancies will be further discussed in Section 6.

In Fig. 8, the calculated and measured sensitivity kernel for the S_2 frequency components is shown, where the calculation is shifted to fit the maximum of the measurement. This will be used as a baseline

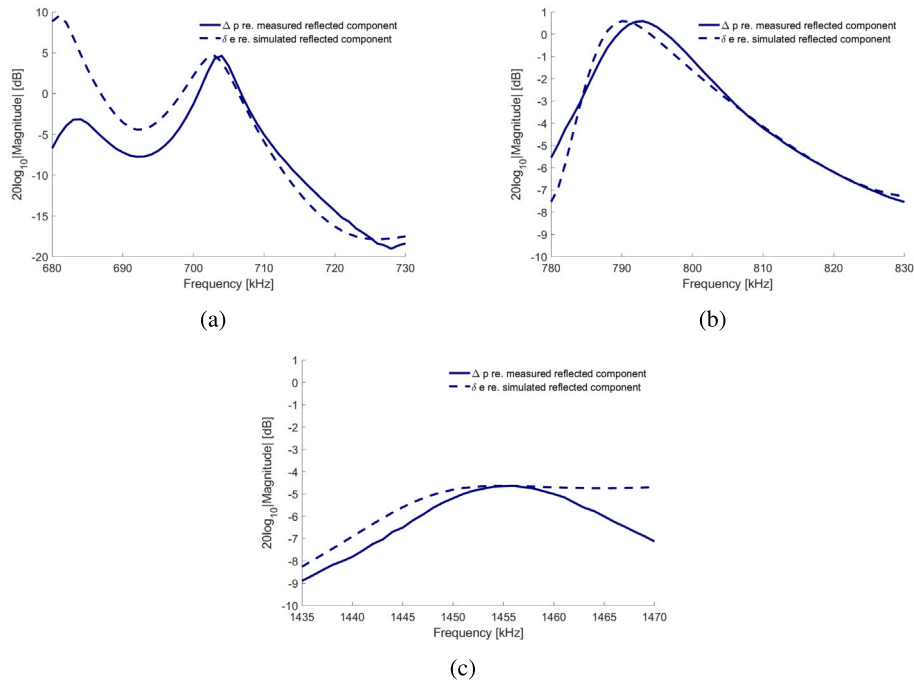


Fig. 7. The ratio of the measured Δp component and the measured reflected component, and the ratio of the calculated δe component and the calculated reflected component, for the three frequency areas, where (a) shows the S_1 frequency area, (b) shows the S_2 frequency area, and (c) shows the A_3 frequency area.

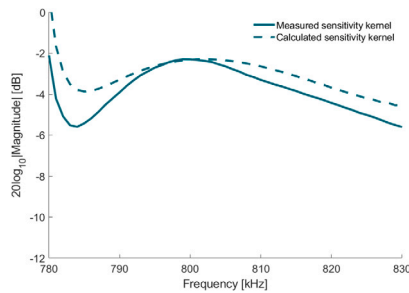


Fig. 8. The measured and calculated sensitivity kernels for the S_2 frequency area. The calculated curve have been shifted to fit the maximum of the measured curve.

reference when predicting the sensitivity of a notch in larger plate thicknesses.

5.4. Notch sensitivity in larger plate thicknesses

In Fig. 9(a) the calculated sensitivity kernel for a 4.02 mm plate and large plate thicknesses are presented as functions of normalized frequency to their respective cut-off frequency for the S_2 mode. The frequency range have been extended to show the behavior before and at the cut-off frequency, and each thickness and respective cut-off frequency are labeled in the legend in Fig. 9(b). The δe component have been normalized to the notch depth (50%) for each plate thickness, and the larger plate thickness sensitivity kernels have been normalized to the maximum above cut-off frequency of the baseline with 4.02 mm thickness. By tracing the curve for the 4.02 mm curve, the maximum sensitivity is at its cut-off frequency and is higher than 1 (0 dB), which is also at a low leaky frequency as indicated in Fig. 9(b). For the larger plate thicknesses, the overall sensitivity varies, while the leaky components decrease with frequency because of the proportionality of sound pressure and frequency. Note however that the sensitivity kernel is a relative measure which means that any dependency on excitation amplitude of the transmitter is removed, whereas an increase of the

amplitude can compensate for the lower leaky magnitude if we set the leaky component of the 4.02 mm plate as a minimum SNR requirement. The larger plate thicknesses also shows a maximum sensitivity at the cut-off frequency, with an additional peak closer to the high leaky frequency area, meaning that if the same setup were applied for larger wall thicknesses, a high crack sensitivity is expected close to the high leaky component. The relative frequency of the sensitivity peak close to the high leaky area from lowest to highest plate thickness are 1.03, 1.049, 1.051, 1.059, 1.062, with the corresponding absolute frequency of 802 kHz, 547 kHz, 411 kHz, 331 kHz and 277 kHz, respectively.

Beyond the high sensitivity observed at the high leaky frequency areas in Fig. 9(a), there is also a high sensitivity of the normalized frequencies lower than the cut-off frequencies, and it is highest for the 6 mm thick plate. In addition, this thickness shows a significant minimum at the normalized frequency just above 1.01. Both of these behaviors are presented more clearly in Fig. 10 where the resolution of the plate thickness range have been set to 0.06 mm and the sensitivity kernels are presented as functions of plate thickness between 4.02 mm to 12 mm and normalized frequency. The high sensitivity before the cut-off frequency is significant for plate thicknesses between 5 mm and 8 mm, with a significant minima just above a normalized frequency of 1.01 for thicknesses roughly between 6 mm and 7 mm. The leaky component for frequencies smaller than cut-off frequency for plate thicknesses between 4.02 mm and 8 mm have been shown in Fig. 9(b) to be relatively low such that a low SNR is expected if attempting exploit the high sensitivity. It is in the same figure also shown that the leaky components just above 1.01 are relatively high, which implies that the minima in Fig. 10 must be due to the δe component being small, indicating that the notch has minimal impact on the leaky Lamb waves at these frequencies and plate thicknesses. The fundamental physics and causes behind both of these behaviors are not known.

A practical challenge with various wall thicknesses is that the diameter of the pipeline may vary in addition [46], such that design considerations may maximize the sensitivity and leaky effect in terms of distance to the pipe wall. We can therefore again exploit the calculations to extrapolate the behavior of an increasing or decreasing standoff as shown in Fig. 11. The frequencies for each curve is the

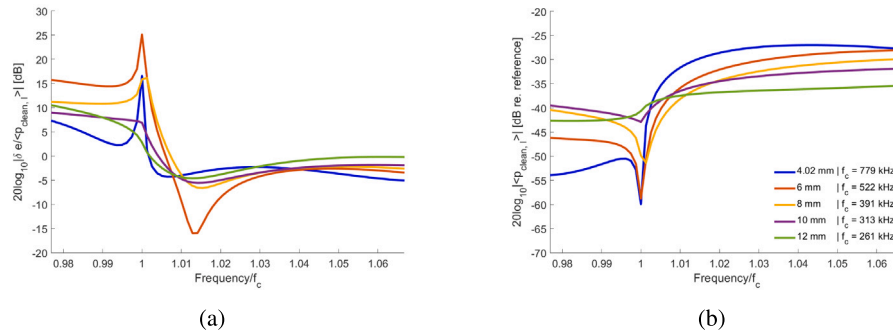


Fig. 9. The calculated sensitivity kernels (a) and calculated leaky components (b) of larger plate thicknesses for the frequencies of S_2 . All curves are normalized to the maximum above cut-off frequency of the curve at 4.02 mm, and the frequency axis is normalized to the cut-off frequency, f_c , of the corresponding plate thickness.

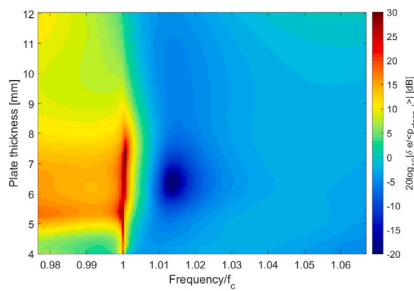


Fig. 10. The calculated sensitivity kernels for the S_2 frequency areas for plate thicknesses between 4.02 mm and 12 mm with resolution of 0.06 mm. All sensitivity kernels have been normalized to the maximum above cut-off frequency of the 4.02 mm plate thickness.

sensitivity peak frequencies close to the high leaky frequency peak observed in Fig. 9(a), which are also marked in the bottom right corner of Fig. 11(b), both relative and absolute. In the sensitivity kernel calculations in Fig. 11(a), it is shown that there is little to gain by increasing the standoff since the sensitivity decreases. It is also clear that decreasing the standoff into the near field of the transmitter will introduce a high variance of sensitivity and leaky component, where the leaky component is shown in Fig. 11(b). These results also indicate that if designing a concept and standoff for, say, a 30 in. pipeline (762 mm), the increased standoff for a 36 in. pipeline (914 mm) may not be an issue in terms of SNR for the leaky component - the magnitude at 200 mm from the plate for all thicknesses shown, has only decayed with roughly 0 to -1 dB compared to 80 mm. In other words, the leaky components of S_2 is strongly conserved over distance in the fluid, which have also been shown for the internal stress and energy in the plate within this frequency range, though in the lateral propagation direction [19]. On the other hand, the sensitivity might decay significantly within this range, down to 8 dB compared to the sensitivity at 80 mm.

For the sake of completeness, the sensitivity kernel as a function of both plate thickness with 0.06 mm resolution and standoff is shown in Fig. 12. It is there shown that the maximum sensitivity, independent of plate thickness, can be expected with standoff at roughly 100 mm.

6. Discussion

We will here discuss the normally incident method for crack detection and potential techniques in optimizing the method further. Following this, it is necessary to discuss the validity of the theoretical sensitivity kernel and the possible sources of error and uncertainties, while also discussing some of the applications that a continued development of the theoretical sensitivity kernel may be used for.

6.1. Notch sensitivity of higher order modes

In Sections 5.2 and 5.4, it was shown that the frequency components of S_2 have both highest leaky components and highest sensitivity from a notch, but it was also shown that a high leaky component does not necessarily introduce a high sensitivity for a notch. The S_2 is highly dominated by shear stress and horizontal particle displacement within the plate, which is also the dominating contributions of the A_0 mode [5]. The S_1 and A_3 modes are highly dominated by the normal components of particle displacement and stress, which indicate a high leakyness and less excitation of shear motion within and the plate, which may be the cause of the less sensitivity of a notch. Lamb modes and types may however have varying sensitivity for different notch depths and sizes [4], which makes it difficult to conclude on applicability of the S_2 mode. Further investigations into depth- and size sensitivity, along with sensitivity for general irregularities (e.g., surface corrosion) would be the natural next steps in the assessment of the normally incident crack detection method.

Furthermore, we have in this paper only focused on the steady state response from a plate with or without a notch in order to have a continuous wave approach to compare directly with the ASM modeling and to avoid any interference between Lamb modes. There are many alternatives to the choice of excitation signal, as for example, its duration or form. One approach to cover a band of leaky Lamb modes, might be to excite a chirp [9,41] from, say, the frequencies of the S_1 mode to the frequencies near the A_3 mode. This might however introduce interference between the modes even if the frequencies are separated in time as with a chirp, since they travel with different group velocities [4] due to dispersion. One could therefore argue that the excitation of a single mode is beneficial, which is also a proposed strategy when applying the fundamental Lamb modes A_0 and S_0 for crack detection [4]. Therefore, if exclusively attempting to apply the S_2 mode for crack detection with the setup suggested in this paper, an optimal choice of excitation signal could be a high amplitude short sine, such that the frequency bandwidth covers both the cut-off frequency and the frequency of maximum leaky component which is shown to also be close to a frequency of high sensitivity. Not only would this signal exhibit a sensitivity for multiple frequencies within this band but can potentially also remove the influence of the specular component, or at least limit its overlap with the leaky component. It would however require thorough investigation, as having too short sine (large bandwidth) can create the said interference between the leaky Lamb modes. The ASM model for the reflection from a clean plate in this paper can be calculated in the time domain in order to optimize a short sine pulse excitation, and it remains to be investigated whether the theoretical sensitivity kernel can predict measurements as shown in this paper but with a short sine instead of a continuous wave approach.

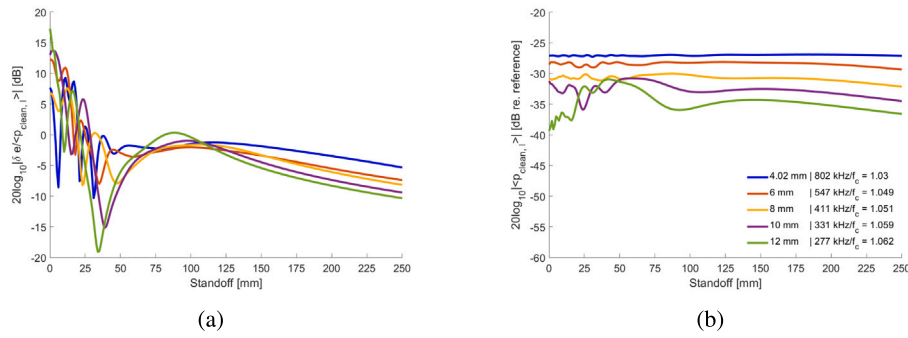


Fig. 11. The calculated sensitivity kernel (a) and calculated clean plate components (b) for a range of standoffs between 0 and 250 mm for the peak sensitivity frequencies of S_2 . All curves have been normalized to the curve of the 4.02 mm plate thickness at 80 mm standoff.

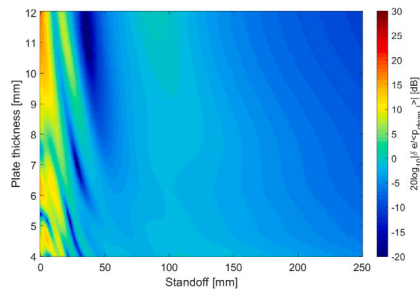


Fig. 12. The calculated sensitivity kernels for the S_2 peak frequency as a function of standoff and plate thickness between 4.02 mm and 12 mm with resolution of 0.06 mm. All sensitivity kernels are normalized to the 4.02 mm plate thickness at 80 mm standoff.

Nevertheless, the work in this paper shows that the S_2 mode is a viable candidate for the normally incident crack detection method in terms of sensitivity and measurable leaky component. By simulations, it was shown that a similar sensitivity as the baseline study can be expected for a range of wall thicknesses, and it was also shown that a compromise between sensitivity and standoff exists in optimizing the system setup. As will be discussed in the next section, when the theoretical sensitivity model is fully validated and commissioned, it can play crucial part in optimizing the method (or potentially other crack detection methods), along with narrowing the scope of measurements necessary for the assessment of applicability.

6.2. Theoretical sensitivity kernel validity and limitations

It is shown Section 5.3 that the theoretical sensitivity kernel of the frequencies of S_2 is able to reasonably predict the measured sensitivity kernel, while showing discrepancies for the frequencies of the S_1 and A_3 modes, perhaps most significantly for the lowest frequencies of the S_1 mode. These discrepancies might be due to the assumption that calculating the theoretical sensitivity kernel as if the plate is twice the distance from the transmitter and receiver is equivalent to the sound pressure at the receiver in fluid in the measurement setup. It is already known that the S_1 mode, when excited by a beam, generate leaky components that vary as they propagate away from the plate [26] (where S_1 is referred to as S_{-2}), though it is only shown for a point receiver on the sound axis of the transmitter. It may however very well be equivalent for the leaky components as the waves propagate along the plate and are received at the lateral receiver, while for the S_2 mode, the leaky component as it propagates from the plate is almost constant (cf. Fig. 11(b)).

Another consideration is that the sensitivity kernel model is based on a variational technique, along with elastodynamic reciprocity and the representation theorem [27], for eigenfunctions in the Earth model [35]. The analogous case for plate geometry would then be the

eigenfunctions of the field variables using the solutions of the dispersion relations [24]. Essentially, these conditions set limitations to the model solutions in the plane wave domain, which in the spatial domain is yet to be determined. It is also utilized as a far-field approximation within the field of seismology, which in the case of plate geometry and the theory presented in this paper, would be the lateral far-field of the propagating waves along the plate. This implies that it may not be valid for the case when a notch is close to the point of impact from the transmitter at the plate or when the notch is close to the receiver. It is however shown in this paper that it provides reasonable results for the frequency components of the S_2 mode for a 50% notch depth when the notch is 20 mm from both the transmitter and receiver, though further investigations to the far-field approximation and depth dependency must be carried out in order to fully appreciate the potentials of this scattering formulation.

Despite the model being exclusively developed for the normally incident method presented in this paper, the fact that it reasonably predicts measurements indicates that it might predict sensitivity for other methods as well. The ASM formulation can be utilized for studies with angled transmitter and receiver (e.g., Anderson et al. [38]), which would allow for sensitivity simulations of, for example, the angled beam approach [16,17], or by exciting the A_0 and S_0 . Validating the model against measurements of these methods could quantify the performance of the normally incident method and sensitivity against benchmarked crack detection methods, though a full comparison would also require further measurements and investigations into sensitivity of, e.g., surface corrosion.

7. Summary and conclusion

We presented a method of crack detection that utilizes the axial symmetric excitation of Lamb waves within the pipe wall such that multiple notch orientations can be detected in a single tool. The leaky Lamb modes S_1 , S_2 and A_3 were excited in a steel plate immersed in water, and the response was measured both with and without a notch (emulating a crack) in the wave path. The performance towards crack detection of the modes was quantified by whether the excited mode returned a large leaky component at the receiver, and the sensitivity for a notch was quantified by the relative difference between the measurement with a notch and without a notch, where the aim was to have a large difference for a frequency corresponding to the frequency of high leaky component. To further investigate the sensitivity from a notch for different measurement parameters and to avoid performing time-consuming measurements, we implemented a theoretical sensitivity kernel from the field of seismology. We compared the model against measurements and established a baseline reference to compare when changing the standoff or plate thickness in the sensitivity kernel calculations.

By investigating the frequency ranges of three leaky Lamb modes – the S_1 , S_2 , and A_3 – it was shown by measurements that the frequency

components of the S_2 mode has the highest leaky component for the system setup and the highest sensitivity close to the high leaky component such that a difference introduced by a notch may be detectable in a noisy environment. Further calculations and measurements into sensitivity of size- and depth dependency of the normally incident method, along with further investigations into optimization of the system setup (e.g., excited pulse length), must however be conducted in order to fully conclude on the applicability the S_2 mode.

It is also shown by calculations of the theoretical sensitivity kernel and by using measurements as baseline, that similar sensitivity characteristics should be expected for higher wall thicknesses, though with a decreasing leaky magnitude due to the proportionality of sound pressure and frequency, and that the standoff can play an important part in optimization of sensitivity. It remains to investigate further limitations of the theoretical sensitivity kernel, as for instance by performing measurements and comparisons of other notch depths, as well as notch sensitivity of larger plate thicknesses in order to validate the calculations presented in this paper. If all limitations and assumptions are thoroughly mapped and investigated, the theoretical sensitivity kernel based on the ASM formulation can be highly advantageous for optimization of crack detection methods and measurement setups.

CRedit authorship contribution statement

Simen Hammervold Midtbø: Conceptualization, Data curation, Formal analysis, Investigation, Methodology, Software, Validation, Visualization, Writing – original draft, Writing – review & editing. **Svein-Erik Måsøy:** Supervision, Writing – review & editing. **Magne Aanes:** Supervision, Writing – review & editing.

Declaration of competing interest

The authors declare that they have no known competing financial interests or personal relationships that could have appeared to influence the work reported in this paper.

Data availability

Data will be made available on request.

Acknowledgments

This work was supported by the Center of Innovative Ultrasound Solutions (CIUS), which receives funding by the Research Council of Norway, project no. 237887. In addition, we would like to thank the Acoustics group at the University of Bergen, Norway, for allowing us to use their directivity measurement system in order to characterize the transducers used in the measurements presented in this paper, and Raymond Larsen with NDT Global for the mechanical configuration of the plate measurement setup.

References

- [1] Y. Bar-Cohen, D.E. Chimenti, Nondestructive evaluation of composite laminates by leaky Lamb waves using a bubbler device, in: J.F. Bussière, J.-P. Monchalán, C.O. Ruud, R.E. Green (Eds.), *Nondestructive Characterization of Materials II*, Springer US, Boston, MA, 1987, pp. 89–93, http://dx.doi.org/10.1007/978-1-4684-5338-6_9.
- [2] D.N. Alleyne, The nondestructive testing of plates using ultrasonic Lamb waves (Ph.D. thesis), Imperial college London, 1991, URL <http://www3.imperial.ac.uk/pls/portallive/docs/1/50531697.PDF>.
- [3] D. Alleyne, M. Lowe, P. Cawley, The inspection of chemical plant pipework using Lamb waves: Defect sensitivity and field experience, in: D.O. Thompson, D.E. Chimenti (Eds.), *Review of Progress in Quantitative Nondestructive Evaluation*, vol. 15A, Springer US, Boston, MA, 1996, pp. 1859–1866, http://dx.doi.org/10.1007/978-1-4613-0383-1_243.
- [4] P.D. Wilcox, M.J.S. Lowe, P. Cawley, Mode and transducer selection for long range Lamb wave inspection, *J. Intell. Mater. Syst. Struct.* 12 (8) (2001) 553–565, <http://dx.doi.org/10.1177/10453890122145348>, URL <https://journals.sagepub.com/doi/abs/10.1177/10453890122145348>.
- [5] M.J.S. Lowe, P. Cawley, J.-Y. Kao, O. Diligent, The low frequency reflection characteristics of the fundamental antisymmetric Lamb wave a_0 from a rectangular notch in a plate, *J. Acoust. Soc. Am.* 112 (6) (2002) 2612–2622, <http://dx.doi.org/10.1121/1.1512702>, URL <https://asa.scitation.org/doi/10.1121/1.1512702>.
- [6] D.N. Alleyne, B. Pavlakovic, M.J.S. Lowe, P. Cawley, Rapid, long range inspection of chemical plant pipework using guided waves, *Key Eng. Mater.* (2004) <http://dx.doi.org/10.4028/www.scientific.net/KEM.270-273.434>, URL <https://www.scientific.net/KEM.270-273.434>.
- [7] L. Satyarnarayan, J. Chandrasekaran, B. Maxfield, K. Balasubramaniam, Circumferential higher order guided wave modes for the detection and sizing of cracks and pinholes in pipe support regions, *NDT E Int.* 41 (1) (2008) 32–43, <http://dx.doi.org/10.1016/j.ndteint.2007.07.004>, URL <http://www.sciencedirect.com/science/article/pii/S0963869507000874>.
- [8] A.A. Swaminathan, B.K. Balasubramaniam, C.I. Anto, K.S. Venkataraman, *Higher Order Mode Cluster (HOMC) Guided Wave Testing Of Corrosion Under Pipe Supports (CUPS)*, 2011, p. 4.
- [9] P. Norli, Ø. Standal, M. Frijlink, F. Prieur, M. Tannerx, K. Haakenstad, Ultrasonic detection of spark eroded notches in steel plates, in: 2017 IEEE International Ultrasonics Symposium (IUS), 2017, pp. 1–5, <http://dx.doi.org/10.1109/ULTSYM.2017.8092503>.
- [10] J. Wang, T. Wang, Q. Luo, A practical structural health monitoring system for high-speed train car-body, *IEEE Access* 7 (2019) 168316–168326, <http://dx.doi.org/10.1109/ACCESS.2019.2954680>, conference Name: IEEE Access.
- [11] S. Livadiotis, A. Ebrahimkhanlou, S. Salamone, Structural Health Monitoring of Pipelines by Means of Helical Guided Ultrasonic Waves and an Algebraic Reconstruction Technique, 2019, <http://dx.doi.org/10.12783/shm2019/32318>.
- [12] M. Castaings, P. Cawley, R. Farlow, G. Hayward, Air-coupled ultrasonic transducers for the detection of defects in plates, in: D.O. Thompson, D.E. Chimenti (Eds.), *Review of Progress in Quantitative Nondestructive Evaluation*, 15A, Springer US, Boston, MA, 1996, pp. 1083–1090, http://dx.doi.org/10.1007/978-1-4613-0383-1_141.
- [13] Transportation Safety Board of Canada, Pipeline Transportation Safety Investigation Report P18H0088 (released 04 March 2020), Tech. rep., URL <https://www.tsb.gc.ca/eng/rappports-reports/pipeline/2018/p18h0088/p18h0088.pdf>.
- [14] T. Beuker, S. Brockhaus, H. Lindner, Overcoming the specific issues associated with the in-line inspection of gas pipelines, Aberdeen, 2010, p. 8, URL <https://ppsa-online.com/papers/10-Aberdeen/2010-07-Rosen.pdf>.
- [15] P.A. Petcher, S. Dixon, Mode mixing in shear horizontal ultrasonic guided waves, *Nondestruct. Test. Eval.* 32 (2) (2017) 113–132, <http://dx.doi.org/10.1080/10589759.2016.1184268>, Publisher: Taylor & Francis, eprint: <http://dx.doi.org/10.1080/10589759.2016.1184268>.
- [16] R. Guajardo, D. Rusu, R. Carmona, C. Rodríguez, Eclipse UCx: Advanced UT Crack Inspection 3 Year Activity Report, 2022, URL <https://www.pipeline-conference.com/abstracts/eclipse-ucx-advanced-ut-crack-inspection-3-year-activity-report>.
- [17] H. Willems, G. Kopp, V. Haro, *Sizing crack indications from ultrasonic ILL: Challenges and options*, Berlin, Germany, 2017.
- [18] M. Castaings, P. Cawley, R. Farlow, G. Hayward, Single sided inspection of composite materials using air coupled ultrasound, *J. Nondestruct. Eval.* 17 (1) (1998) 37–45, <http://dx.doi.org/10.1023/A:1022632513303>.
- [19] S.H. Midtbø, M. Aanes, A.S. Talberg, S.-E. Måsøy, ASM and finite beam description of the excited leaky Lamb wave fields in a fluid-immersed plate, *Ultrasonics* 127 (2023) 106845, <http://dx.doi.org/10.1016/j.ultras.2022.106845>, URL <https://www.sciencedirect.com/science/article/pii/S0041624X22001512>.
- [20] J. Rose, Guided wave nuances for ultrasonic nondestructive evaluation, *IEEE Trans. Ultrason. Ferroelectr. Freq. Control* 47 (3) (2000) 575–583, <http://dx.doi.org/10.1109/58.842044>, conference Name: IEEE Transactions on Ultrasonics, Ferroelectrics, and Frequency Control.
- [21] M.J.S. Lowe, O. Diligent, Low-frequency reflection characteristics of the s_0 Lamb wave from a rectangular notch in a plate, *J. Acoust. Soc. Am.* 111 (1) (2002) 64–74, <http://dx.doi.org/10.1121/1.1424866>, URL <https://asa.scitation.org/doi/10.1121/1.1424866>.
- [22] B. Auld, *Acoustic Fields and Waves in Solids*, second ed., vol. 2, Krieger Publishing Company, Malabar, Florida, 1990.
- [23] L.R.F. Rose, B.S. Vien, W.K. Chiu, Analytical solutions for crack-like scatterers and sources in isotropic elastic plates, *Wave Motion* 93 (2020) 102476, <http://dx.doi.org/10.1016/j.wavemoti.2019.102476>, URL <http://www.sciencedirect.com/science/article/pii/S0165212519300022>.
- [24] M. Aanes, Interaction of Piezoelectric Transducer Excited Ultrasonic Pulsed Beams with a Fluid-Embedded Viscoelastic Plate. Finite Element Modeling, Angular Spectrum Modeling and Measurements, The University of Bergen, 2014, URL <https://bora.uib.no/handle/1956/7891>.
- [25] M. Aanes, K.D. Lohne, P. Lunde, M. Vestrheim, Beam diffraction effects in the backward wave regions of viscoelastic leaky Lamb modes for plate transmission at normal incidence, *IEEE Trans. Ultrason. Ferroelectr. Freq. Control* 64 (10) (2017) 1558–1572, <http://dx.doi.org/10.1109/TUFFC.2017.2719627>, conference Name: IEEE Transactions on Ultrasonics, Ferroelectrics, and Frequency Control.

- [26] M.M. Sørther, S.H. Midtbø, P. Lunde, Interaction of three-dimensional acoustic beam with fluid-loaded solid plate: Axial near- to far-field transmission at normal beam incidence, *Ultrasonics* 125 (2022) 106795, <http://dx.doi.org/10.1016/j.ultras.2022.106795>, URL <https://www.sciencedirect.com/science/article/pii/S0041624X22001019>.
- [27] K. Aki, P.G. Richards, *Quantitative Seismology*, second ed., University Science Books, 2002, Google-Books-ID: pWhePgAACAAJ.
- [28] R. Snieder, The influence of topography on the propagation and scattering of surface waves, *Phys. Earth Planet. Inter.* 44 (3) (1986) 226–241, [http://dx.doi.org/10.1016/0031-9201\(86\)90072-5](http://dx.doi.org/10.1016/0031-9201(86)90072-5), URL <https://www.sciencedirect.com/science/article/pii/0031920186900725>.
- [29] R. Snieder, 3-D linearized scattering of surface waves and a formalism for surface wave holography, 1986, <http://dx.doi.org/10.1111/j.1365-246X.1986.tb04372.x>.
- [30] F.A. Dahlen, The spectra of unresolved split normal mode multiplets, *Geophys. J. R. Astron. Soc.* 58 (1) (1979) 1–33, <http://dx.doi.org/10.1111/j.1365-246X.1979.tb01008.x>, URL <https://onlinelibrary.wiley.com/doi/abs/10.1111/j.1365-246X.1979.tb01008.x>.
- [31] F.A. Dahlen, J. Tromp, *Theoretical Global Seismology*, Princeton University Press, 1998, google-Books-ID: GWnuBws5gBEC.
- [32] F.A. Dahlen, S.-H. Hung, G. Nolet, Fréchet kernels for finite-frequency traveltimes—I. Theory, *Geophys. J. Int.* 141 (1) (2000) 157–174, <http://dx.doi.org/10.1046/j.1365-246X.2000.00070.x>, URL <https://academic.oup.com/gji/article/141/1/157/578991>.
- [33] Y. Zhou, F.A. Dahlen, G. Nolet, Three-dimensional sensitivity kernels for surface wave observables, *Geophys. J. Int.* 158 (1) (2004) 142–168, <http://dx.doi.org/10.1111/j.1365-246X.2004.02324.x>, URL <https://onlinelibrary.wiley.com/doi/abs/10.1111/j.1365-246X.2004.02324.x>.
- [34] K. Yoshizawa, B.L.N. Kennett, Sensitivity kernels for finite-frequency surface waves, *Geophys. J. Int.* 162 (3) (2005) 910–926, <http://dx.doi.org/10.1111/j.1365-246X.2005.02707.x>, URL <https://academic.oup.com/gji/article/162/3/910/589235>. Publisher: Oxford Academic.
- [35] L. Zhao, F.A. Dahlen, Mode-sum to ray-sum transformation in a spherical and an aspherical earth, *Geophys. J. Int.* 126 (2) (1996) 389–412, <http://dx.doi.org/10.1111/j.1365-246X.1996.tb05299.x>, URL <https://academic.oup.com/gji/article/126/2/389/623643>.
- [36] R. Johnson, A. Devaney, Transducer model for plate thickness measurement, in: 1982 Ultrasonics Symposium, 1982, pp. 502–504, <http://dx.doi.org/10.1109/ULTSYM.1982.197877>.
- [37] D.P. Orofino, P.C. Pedersen, Evaluation of angle-dependent spectral distortion for infinite, planar elastic media via angular spectrum decomposition, *J. Acoust. Soc. Am.* 93 (3) (1993) 1235–1248, <http://dx.doi.org/10.1121/1.405408>, URL <https://asa.scitation.org/doi/10.1121/1.405408>. Publisher: Acoustical Society of America.
- [38] M.J. Anderson, P.R. Martin, C.M. Fortunko, Resonant transmission of a three-dimensional acoustic sound beam through a solid plate in air: Theory and measurement, *J. Acoust. Soc. Am.* 98 (5) (1995) 2628–2638, <http://dx.doi.org/10.1121/1.413229>, URL <https://asa.scitation.org/doi/10.1121/1.413229>.
- [39] D.E. Chimenti, Guided waves in plates and their use in materials characterization, *Appl. Mech. Rev.* 50 (5) (1997) 247–284, <http://dx.doi.org/10.1115/1.3101707>.
- [40] E.G. Williams, *Fourier Acoustics: Sound Radiation and Nearfield Acoustical Holography*, Academic Press, 1999, google-Books-ID: vjfkLFBgMeIC.
- [41] G. Waag, L. Hoff, P. Norli, Air-coupled ultrasonic through-transmission thickness measurements of steel plates, *Ultrasonics* 56 (2015) 332–339, <http://dx.doi.org/10.1016/j.ultras.2014.08.021>, URL <https://www.sciencedirect.com/science/article/pii/S0041624X14002431>.
- [42] A. Bernard, M.J.S. Lowe, M. Deschamps, Guided waves energy velocity in absorbing and non-absorbing plates, *J. Acoust. Soc. Am.* 110 (1) (2001) 186–196, <http://dx.doi.org/10.1121/1.1375845>, URL <https://asa.scitation.org/doi/10.1121/1.1375845>.
- [43] J.D. Achenbach, *Wave Propagation in Elastic Solids*, Noth-Holland publishing company, 1973.
- [44] J.M. Carcione, Energy balance and fundamental relations in dynamic anisotropic poro-viscoelasticity, *Proc. R. Soc. Lond. Ser. A Math. Phys. Eng. Sci.* 457 (2006) (2001) 331–348, <http://dx.doi.org/10.1098/rspa.2000.0669>, URL <https://royalsocietypublishing.org/doi/10.1098/rspa.2000.0669>. Publisher: Royal Society.
- [45] P. Roux, C. Marandet, B. Nicolas, W.A. Kuperman, Experimental measurement of the acoustic sensitivity kernel, *J. Acoust. Soc. Am.* 134 (1) (2013) EL38–EL44, <http://dx.doi.org/10.1121/1.4808111>, URL <https://asa.scitation.org/doi/full/10.1121/1.4808111>.
- [46] S.D. Palkovic, S.C. Bellemare, K.K. Botros, X.D. Chen, R. Kania, Calibration of a nondestructive toughness tester (NDTT) for measuring fracture toughness of pipeline steel, *American Society of Mechanical Engineers Digital Collection*, 2018, <http://dx.doi.org/10.1115/IPC2018-78538>, URL <http://dx.doi.org/10.1115/IPC2018-78538.1792>.